HEALTH AND MEDICINE

Reversibly photoswitchable protein assemblies with collagen affinity for in vivo photoacoustic imaging of tumors

Shuai Chen†, Kaixin Li†, Xin Chen, Shan Lei, Jing Lin, Peng Huang*

Recent advancements in photoacoustic (PA) imaging have leveraged reversibly photoswitchable chromophores, known for their dual absorbance states, to enhance imaging sensitivity through differential techniques. Yet, their deployment in tumor imaging has faced obstacles in achieving targeted delivery with high efficiency and specificity. Addressing this challenge, we introduce innovative protein assemblies, DrBphP-CBD, by genetically fusing a photosensory module from *Deinococcus radiodurans* bacterial phytochrome (DrBphP) with a collagen-binding domain (CBD). These protein assemblies form sub-100-nanometer structures composed of 24 DrBphP dimers and 12 CBD trimers, presenting 24 protein subunits. Their affinity for collagens, combined with impressive photoswitching contrast, markedly improves PA imaging precision. In various tumor models, intravenous administration of DrBphP-CBD has demonstrated enhanced tumor targeting and retention, augmenting contrast in PA imaging by minimizing background noise. This strategy underscores the clinical potential of DrBphP-CBD as PA contrast agents, propelling photoswitchable chromoproteins to the forefront of precise cancer diagnosis.

INTRODUCTION

Photoacoustic (PA) imaging is a non-ionizing hybrid technique combining the high optical contrast of optical imaging with the superior ultrasonic spatial resolution in deep tissues, thus addressing the limitations of both pure optical and ultrasound imaging (*1–4*). Its unique capability for label-free imaging at various scales sets PA imaging apart from other modalities. Recent advancements have focused on enhancing image contrast and disease monitoring by developing exogenous contrast agents to heighten signal-to-noise ratio (SNR) (*5–10*). However, inherent challenges, prominently, the absorption by endogenous chromophores, such as hemoglobin and melanin, introduce considerable background noise, undermining the sensitivity of PA imaging. Overcoming these limitations is essential to maximize PA imaging's clinical potential.

Recent progress in multiscale PA imaging has underscored the potential of reversibly photoswitchable chromophores (*11–17*), notably bacterial phytochromes (BphPs). These genetically encoded photoabsorbers bind to the biliverdin (BV) IXα chromophore (*18, 19*). They are capable of switching between red and near-infrared (NIR) light absorption states and resist photobleaching, making them ideal for longitudinal imaging. By subtracting PA images captured in two different states, this photochromic property helps eliminate extraneous background noise. This technique, termed background-suppressed PA imaging, is particularly promising for identifying deep-seated tumors. Current methods, like injecting tumor cells expressing these proteins directly into targeted sites (*11, 12*), have been successful in studies but are impractical for clinical use. In addition, Gao *et al.* (*15*) and Chee *et al.* (*20*) have devised bacterial-based systems for precise tumor delivery of genetically encoded photochromic chromoproteins. However, to routinely use these photochromic chromoproteins for efficient

tumor-targeted, contrast-enhanced imaging, the development of more systematic delivery methods with enhanced efficiency and specificity becomes necessary.

Engineered nanoparticles (NPs) can endow imaging techniques with enhanced signal sensitivity, better spatial resolution, and the ability to relay information about biological systems at the molecular and cellular levels (*21–26*). NPs that surpass the renal clearance threshold tend to accumulate in solid tumors due to the enhanced permeability and retention (EPR) effect, a result of tumors' porous vasculature and impaired lymphatic drainage. Protein self-assembled NPs, in particular, are advantageous for bioimaging and cancer therapy (*27–32*). They exhibit excellent self-assembly, composition, reproducibility, aqueous solubility, high cellular uptake, and biocompatibility (*33–36*). Their bioengineering adaptability allows for the incorporation of various functional groups without needing chemical synthesis or toxic solvents (*37, 38*). Moreover, proteins' natural amphipathicity enables their hydrophobic domains to bind effectively to hydrophobic antitumor drugs or imaging probes, thus enhancing loading capacity. Recently, protein assemblies like ferritin, heat shock proteins, and gas vesicles have been explored for imaging applications in various cancers, cardiovascular diseases, and brain imaging using multiple modalities (*39*). However, the field of engineering ideal bioimaging protein assemblies, still less explored, offers numerous opportunities for development. BphPs are characteristically organized into a dimeric quaternary structure, where the constituent protomers are intricately aligned in either parallel or antiparallel orientations, facilitated by extensive helical bundles (*40*), suggesting their potential for the development of BphPs-based self-assemblies. While BphPs maintain efficiency in deep tissues, its effectiveness in tumor targeting is limited by the absence of specific binding sites.

Collagen, the predominant protein within mammalian extracellular matrices, remains generally inaccessible due to the low permeability characteristic of intact vascular systems (*41*). However, the aberrant vascular architecture of neoplastic tissues confers increased permeability, rendering collagen exposed to the systemic circulation. This abnormal exposure, combined with collagen's overexpression in various cancers, presents it a unique target for medical imaging

Marshall Laboratory of Biomedical Engineering, International Cancer Center, Laboratory of Evolutionary Theranostics (LET), School of Biomedical Engineering, Shenzhen University Medical School, Shenzhen University, Shenzhen, 518055, China.
*Corresponding author. Email: peng.huang@szu.edu.cn
†These authors contributed equally to this work.

(*42*, *43*). Prior research has substantiated the efficacy of engineered cytokines and monoclonal antibodies that exhibit collagen affinity in mediating the selective localization and retention of therapeutic agents within the tumor stroma (*44*–*51*). Specifically, the collagen-binding domain (CBD) of von Willebrand factor has demonstrated a pronounced affinity toward type I and III collagen, which are prolific within the tumor matrix (*44*, *45*, *51*–*53*). Despite the advantages conferred by passive targeting mechanisms in NPs delivery to tumor sites, challenges persist regarding the heterogeneity of intratumoral distribution and the temporality of NPs retention (*54*). We propose that fusing CBD with BphPs may confer a targeted delivery of PA contrast agents to the tumor microenvironment (TME), ensuring their physical entrapment and enhancing the localized bioavailability of BphPs, thereby optimizing their diagnostic imaging potential.

Harnessing the robust photoswitching capabilities of BphPs and the high collagen affinity of CBD, we have synthesized distinctive protein assemblies, DrBphP-CBD. This innovative construct is engineered by recombinantly fusing N-terminal photosensory module from *Deinococcus radiodurans* bacterial phytochrome (DrBphP) with CBD. Departing from traditional homomeric self-assembly paradigms exemplified by ferritin, this dual-functional assembly comprises 24 DrBphP dimers and 12 CBD trimers, self-assembling into structures with 24 iterations of each subunit and an average size of 74 nm. The resulting DrBphP-CBD are designed to exploit the abnormal vascular architecture of tumors, adhering to the accessible collagens. This specificity facilitates sustained delivery, high retention, and heightened photoswitching contrast of DrBphP within TME. In vivo studies across various mouse models have shown preferential targeting and retention of DrBphP-CBD in tumor tissue postintravenous injection and further enhanced PA imaging by markedly attenuating background signal. Collectively, these findings indicated that DrBphP-CBD can be used as a versatile platform for delivering reversibly photoswitchable chromoproteins, providing a universal approach for precise cancer detection via collagen targeting. Furthermore, our study exhibits the potential of DrBphP-CBD as a formidable PA contrast agent in clinical diagnostics and paves the way for advancements in precise, photoswitchable chromoprotein-based PA imaging methodologies in the oncological arena.

RESULTS AND DISCUSSION
Design and characterization of DrBphP-CBD assemblies
The precise self-assembly of protein monomers into ordered nanostructures heralds the synthesis of advanced materials with versatile functional profiles (*55*). Proteins in nature have adapted to form symmetrical oligomeric complexes, an intrinsic characteristic that has been harnessed through the integration of oligomers with varying symmetries to fabricate intricate protein nanostructures. It has been indicated that the genetic fusion of protein monomers with differing oligomeric states along a structured α helix can inform the prediction and design of the resultant protein self-assembly process (*56*).

BphPs are distinguished by their unique photochemical characteristics, including dual red- and NIR-absorbing states for deep tissue imaging, noncytotoxicity, selective endogenous BV binding, and low photoswitching fatigue (*11*). While BphPs maintain efficiency in deep tissues, their effectiveness in tumor targeting is hindered by the absence of specific binding sites. By integrating strategies for tumor stroma binding and using genetic engineering techniques, CBD can be fused as a functional module to enhance BphPs' specificity for collagen targeting and retention within tumor tissues.

The full-length DrBphP1, consisting of 755 amino acids, is characterized by an N-terminal photosensory module (PSM; residues 1 to 594) that binds the BV chromophore autocatalytically to a conserved cysteine residue and a C-terminal variable output module (OM; residues 595 to 755) responsible for initiating cellular responses (*18*). An elongated helical structure extends the overall length of DrBphP1 to 15.8 nm, with dimensions measuring 5.2 nm in width and 4.2 nm in height. DrBphP1 typically exists in a dimeric conformation, wherein protomers are intricately aligned in either parallel or antiparallel orientations (*18*, *19*, *40*). In our design, the PSM domain of DrBphP1, denoted as DrBphP, is conserved while the OM domain has been replaced with CBD to endow DrBphP with specific tumor-targeting attributes. A flexible loop has been introduced to facilitate the modular architecture. Computational modeling via AlphaFold2 (*57*) reveals that the chimeric DrBphP-CBD fusion protein retains the original length of 15.8 nm and height of 4.2 nm while expanding in width to 8.6 nm. (Fig. 1A). Despite the absence of an experimentally resolved structure for the truncated DrBphP, AlphaFold-Multimer (*58*) simulations suggest that DrBphP maintains its ability to form a stable dimer, with the most favorable model achieving a template modeling (TM) score of 0.766, suggesting a tight association between two monomers via hydrogen bonds and hydrophilic interaction (Fig. 1B and fig. S1A). Furthermore, the predicted trimerization potential of CBD, evidenced by a TM score of 0.539 for the leading model, indicates the formation of a stable trimeric interface via hydrogen bonds (Fig. 1C and fig. S1B). As depicted in Fig. 1D, this architectural innovation enables the self-assembly of DrBphP-CBD into an intricate nanostructure, comprising 24 DrBphP dimers and 12 CBD trimers, thus forming a complex with 24 copies of each protein subunit. This results in a supramolecular entity that exhibits formidable dimensions, stretching to a length and width of 65 nm while maintaining a consistent height of 4.2 nm.

On the basis of this computation, DrBphP-CBD was constructed and synthesized in *Escherichia coli* BL21 strain, isolated from cellular lysates via nickel–nitrilotriacetic acid immobilized metal affinity chromatography (IMAC), and further purified by size exclusion chromatography (SEC). Subsequent characterization of the purified protein was conducted using SDS–polyacrylamide gel electrophoresis (SDS-PAGE). As shown in Fig. 2A, DrBphP-CBD elute at a volume of approximately 50 ml, SDS-PAGE analysis revealed a single protein band corresponding to ~87 kDa under reducing conditions, suggestive of the protein's purity. The dimension of the protein assemblies was determined using dynamic light scattering (DLS), which revealed an average hydrodynamic diameter of 74 nm (Fig. 2B). The morphology of these protein nanostructures was observed by transmission electron microscopy (TEM), confirming the formation of highly uniform spherical structures with an average diameter of approximately 80 nm, a dimension that is concordance with the DLS measurements (Fig. 2C). In addition, atomic force microscopy (AFM) was used to assess the surface topography of DrBphP-CBD, revealing an estimation of the particle dimensions at approximately 70 nm in diameter and a height of 4 nm (Fig. 2, D to F). These results corroborate the theoretical structural models previously delineated (Fig. 1D), thus validating the predictive design framework used in the development of these protein assemblies.
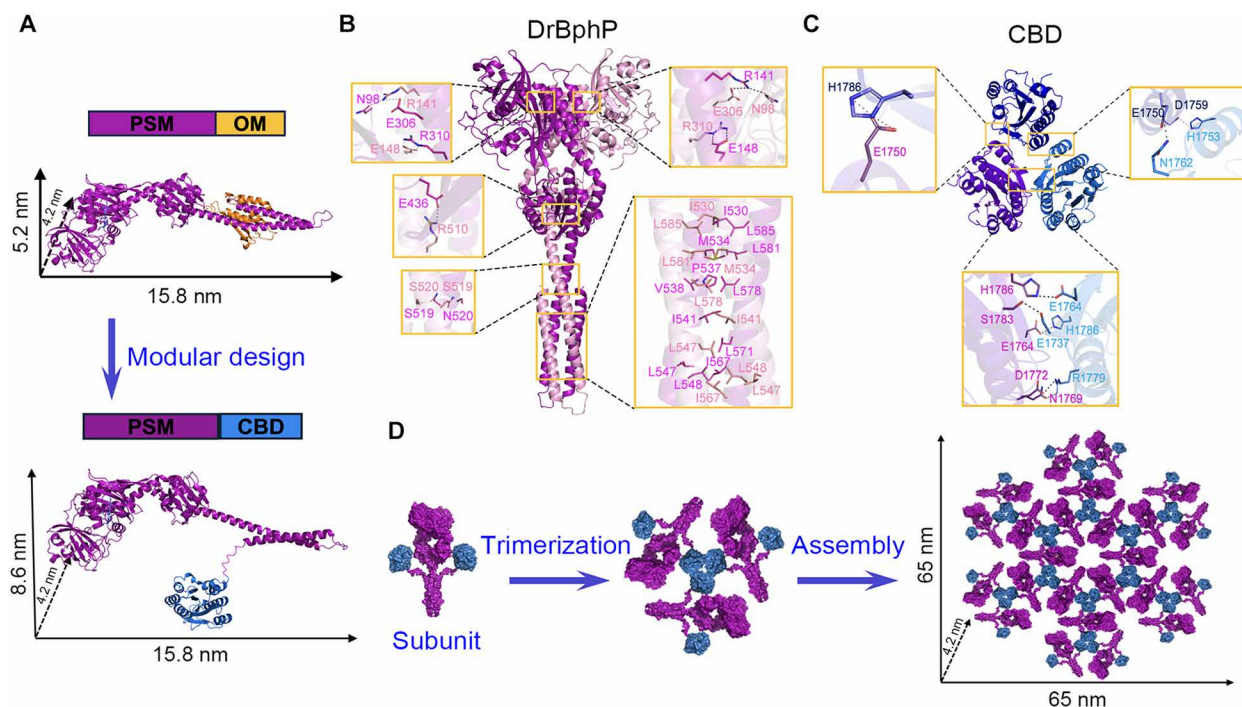
Fig. 1. Rational design of DrBphP-CBD assemblies. (**A**) The schematic and structural representation of DrBphP1 with a PSM in magentas and a C-terminal OM in orange. The OM is replaced by the CBD module (marine) to create the DrBphP-CBD construct. (**B**) Dimeric structural model of DrBphP. (**C**) Predicted trimer formation by the CBD. (**D**) Illustration of the in vitro self-assembly of DrBphP-CBD, each incorporating 24 DrBphP dimers and 12 CBD trimers, forming a complex with 24 copies of each protein subunit.

DrBphP-CBD efficiently localize within tumors after intravenous injection

The interaction sites between CBD and type III collagen have been resolved (59); however, the binding domain for type I collagen remains elusive. Using AlphaFold-Multimer predictions, the interaction between CBD and type I collagen shows a high TM score of 0.847, indicative of a robust binding affinity (Fig. 3A and fig. S1C). This score parallels the identified binding region for type III collagen, hinting at a common binding interface within the CBD sequence ($_{1737}$SITTIDVPWNVVPEKAHLLSLVDVMQREGGPSQ IGDALGFAVRYLTSEMHG$_{1787}$). Furthermore, the central area of the predicted CBD trimer, enriched with collagen-binding sites, aligns with this interface, suggesting that the designed higher-order protein assemblies may have stronger collagen-binding capabilities (Fig. 3B).

To substantiate this hypothesis, we evaluated the in vitro binding affinity of DrBphP-CBD toward recombinant collagens using indirect enzyme-linked immunosorbent assay (ELISA). These assays demonstrated an increased affinity of DrBphP-CBD for type I and III collagen, evidenced by dissociation constants (K_d) of 0.48 nM and K_d = 26.45 nM, respectively (Fig. 3C). In contrast, DrBphP lacking CBD exhibited no specific affinity for collagens. Subsequently, we examined in vivo distribution of DrBphP-CBD. Second-harmonic generation (SHG) microscopy has become a pivotal modality for imaging collagen content and structure across various tissues. This intrinsic signal technique requires no extrinsic dyes, providing exceptional sensitivity to changes in collagen structure relevant to diseases like cancer and fibrosis (60, 61). Initial validation of collagen distribution across various tumor phenotypes was performed using intravital SHG imaging with a laser scanning two-photon microscope (IVM-MS2, IVIM Technology). As shown in fig. S2, variability in SHG signals correlated with collagen density, specifically MC38 and MDA-MB-231 tumors, exhibited high collagen content with corresponding SHG signals, whereas the 4T1 tumor type was characterized by lower collagen density and SHG signals. The DrBphP-CBD exhibits red fluorescence emission with excitation at 684 nm and an emission peak at 725 nm (fig. S3). The time-dependent red fluorescence signals of MC38 tumor sites were subsequently monitored following a single intravenous injection of DrBphP-CBD, along with SHG images of collagen. As demonstrated in Fig. 3D, a marked increase in the concentration of DrBphP-CBD was observed within tumors at 4 hours postinjection (p.i.), relative to DrBphP. This accumulation peaked between 6 and 10 hours p.i. Corresponding observations were also noted in the 4T1 tumor models (fig. S4). However, the fluorescence intensity of DrBphP-CBD was attenuated because of the diminished collagen content within these tumors. The results highlighted the superior active targeting capability of DrBphP-CBD compared to DrBphP alone. Complementary intravital microscopy and histopathological assessments further confirmed the colocalization of DrBphP-CBD with collagens within the tumor matrix (Fig. 4 and fig. S5). These findings elucidate that DrBphP-CBD exhibit the intended functionality, demonstrating an ability to bind with high affinity to type I and III collagen. Notably, this affinity translates into a markedly superior targeting and retention of DrBphP-CBD within the tumor matrix when contrasted with DrBphP alone.
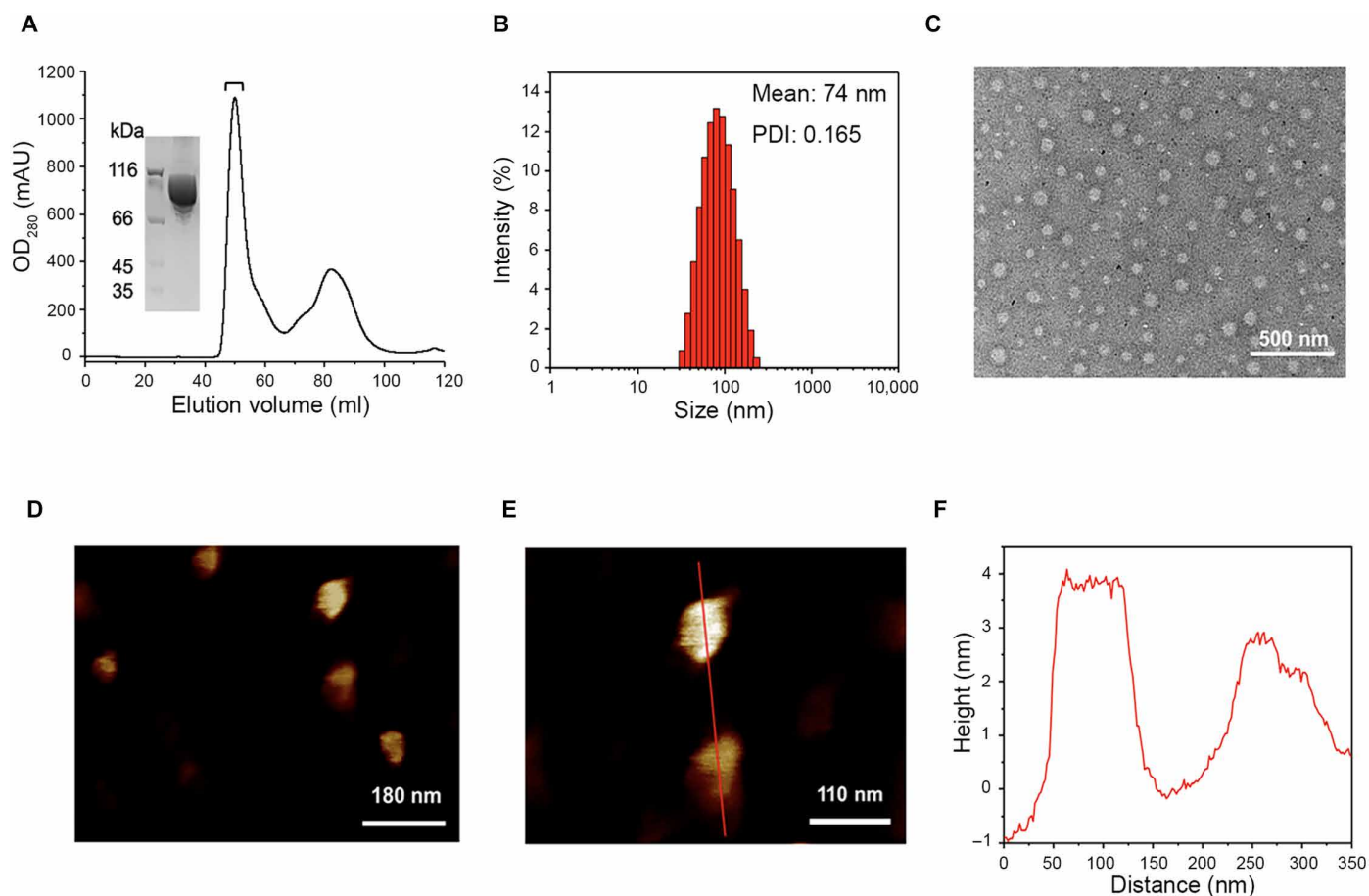
Fig. 2. Characterization of DrBphP-CBD. (**A**) SEC profile of purified DrBphP-CBD from a Superdex 200 16/600 column and corresponding SDS-PAGE analysis (inset). (**B**) Determination of average hydrodynamic diameter of DrBphP-CBD via DLS. (**C**) Visualization of DrBphP-CBD using negative stain TEM. (**D** and **E**) The morphology of DrBphP-CBD determined by AFM. (**F**) Height profile analysis along a designated line in (E). OD280, optical density at 280 nm. mAU, milli-absorbance units. PDI, polydispersity index.

DrBphP-CBD preserve superior reversibly photoswitchable capability

Reversible photoswitching represents a crucial characteristic of BphPs for PA imaging, facilitating the enhancement of image contrast through differential imaging. As reported (*11*), BphPs undergo photoconversion due to the cis-trans photoisomerization of its D-ring of the covalently bonded BV chromophore. This isomerization results in two distinct absorption states: the OFF state (Pr) absorbing within the 630- to 690-nm range and the ON state (Pfr) absorbing within the 730- to 808-nm range (Fig. 5A).

The comparable innate photochromic properties of DrBphP-CBD and DrBphP are observed when it transitions from the Pr to the Pfr state under 635-nm light illumination and reversely from Pfr to Pr under 808-nm light illumination (Fig. 5B and fig. S6). The contrast generated through photoswitching is pivotal for enhancing imaging specificity and suppressing background interference. This contrast is quantified by the ratio of the absorption coefficients in the ON state to those in the OFF state, where a higher ratio signifies an improved maintenance of the signal intrinsic to the chromoprotein upon the removal of background signals, thus optimizing image contrast in differential PA imaging. As detailed in Fig. 5B, there

are obvious changes in the spectral absorption characteristics of DrBphP-CBD between its two states, with the absorption coefficient ratio (Pfr/Pr) being approximately 11 at 760 nm, indicative of an exceptional photoswitching contrast. As illustrated in Fig. 5C, the differential image obtained by subtracting the OFF-state from the ON-state PA images at 760 nm exhibits substantially enhanced contrast. To simulate a deep biological tissue environment, tube tests were conducted within chicken breast tissues (fig. S7). Comparable images were noted in the 10-mm-thick sample (fig. S7 and Fig. 5C), suggesting the feasibility of PA imaging with markedly reduced background signals at deep tissue depth, such as those encountered in solid tumors, potentially achievable using DrBphP-CBD. As demonstrated in Fig. 5 (D and E), multiple cycles of photoactivation were successfully achieved through alternating exposure to 760- and 635-nm wavelengths. Notably, these repeated switching cycles did not result in photoswitching fatigue or photobleaching. Photobleaching resistance is pivotal in PA imaging, ensuring the durability and stability of imaging agents. This stability is crucial for consistent, precise, and reproducible imaging over extended periods, enhancing both the sensitivity and safety of the imaging procedure, particularly in deep tissue examinations and during prolonged imaging
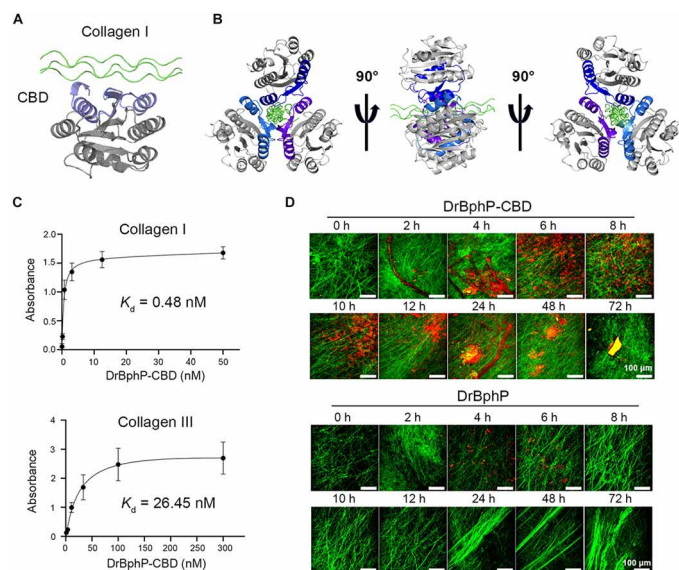
Fig. 3. Tumor localization of DrBphP-CBD via collagen affinity. (**A** and **B**) Computational model of the interaction between CBD and type I collagen. The binding interface of CBD with type I collagen is highlighted. (**C**) Quantification of the dissociation constant (K_d) for DrBphP-CBD against type I and III collagen via ELISA assay. (**D**) Sequential in vivo imaging of DrBphP-CBD and DrBphP accumulation in MC38 tumor tissues, paired with collagen visualization via second-harmonic generation (SHG). Scale bars, 100 μm.

sessions. Moreover, the photoswitchable functionality of DrBphP-CBD between the ON and OFF states was effectively maintained, even at increased depths, with transitions from the ON to OFF state completing within 6 s during data acquisition at 760 nm. Subsequent irradiation with a 635-nm laser for 10-s post-OFF state facilitated a complete reversion to the ON state. The switching ratio only diminished from 3.67 ± 0.21 at a depth of 0 mm to 2.6 ± 0.14 at 10 mm, thereby verifying the consistent and reversible photoswitching capability of DrBphP-CBD and the reproducibility of the imaging technique. Enhanced image contrast was observed after the subtraction of the two states. As illustrated in Fig. 5F, the SNR of differential image displayed a 20-fold increase compared to the original ON state in a water medium and a 17.7-fold enhancement in chicken breast tissue at a depth of 10 mm. These findings corroborate the high photoswitching efficiency between the two states in deep tissues, reaching up to a centimeter scale. In addition, DrBphP-CBD were found to remain stable when exposed to 715-nm laser pulses, thus supporting 3D PA imaging with the Vevo LAZR-X system.

DrBphP-CBD enable contrast-enhanced PA imaging in multiple solid tumor models

To elucidate the targeted tumor accumulation, retention in the TME, and the efficacy of the contrast enhancement in PA imaging, DrBphP-CBD were administered systematically to a series of murine models bearing MC38, MDA-MB-231, and 4T1 tumors. Control group was set by using corresponding tumor-bearing mice injected intravenously with DrBphP. Signal accumulation of DrBphP-CBD within tumor tissues was visualized via PA imaging, which involved the differential subtraction of the "OFF" state from the "ON" state signals, thereby isolating the photoswitchable signal of the DrBphP-CBD. A temporal assessment of PA imaging was conducted on the

tumor-bearing mice, capturing images before and at various intervals following DrBphP-CBD administration, specifically at 2, 4, 6, 8, 10, 12, 24, 48, and 72 hours. This allowed for a comprehensive analysis of the DrBphP-CBD's targeting proficiency and retention within tumor tissues over time.

The acquired imaging data from a representative subcutaneous MC38 tumor mouse model, specifically highlighting the B-scans of ON and OFF states and their differential images, were shown in Fig. 6A. Initial accumulations of DrBphP-CBD were observed at 4 hours p.i. The PA signals of these protein assemblies within the tumor tissues notably intensify, reaching a peak at 10 hours p.i. and sustaining over a 72-hour duration. Conversely, the PA signals of DrBphP alone were discernible within tumor tissues at 4 to 6 hours p.i. and thereafter diminishing and vanishing at 8 hours, presumably due to the efflux of DrBphP from tumor tissues. The mice administered with DrBphP-CBD exhibited PA signals with a 2.3-fold increase in amplitude as compared to those treated with DrBphP at the 4-hour interval. These data suggest that DrBphP-CBD have an enhanced propensity for tumor targeting and exhibit prolonged retention within TME. 3D rendered images were used to delineate the 715-nm PA signals within tumor tissues, the homogeneity of intratumoral distribution of DrBphP-CBD was evidenced by the uniform illumination of the entire tumor region (Fig. 6B). The biodistribution of these protein assemblies, as elucidated by ex vivo PA imaging of organs at 10 hours p.i., indicated a predominant tumor accumulation, followed by other organ localization (Fig. 6C), thereby confirming the specificity of the DrBphP-CBD for tumor targeting.

Subsequent studies were conducted on breast tumor models. In the MDA-MB-231 xenografted model, DrBphP-CBD were detectable within tumor tissues as early as 2 hours p.i. The PA signals exhibited a progressive increase over the subsequent 10 hours, reaching a plateau at 12 hours, and was still visible at 72 hours (Fig. 7A and fig. S8). The 4T1 tumor model exhibited analogous results to the MC38 model; however, the PA amplitude in 4T1 tumor–bearing mice treated with DrBphP-CBD was discernibly weaker than that observed in the MC38 tumor-bearing mice (Fig. 7B and fig. S9). Despite this, our quantitative analysis across three different tumor types showed that DrBphP-CBD was detectable in tumor tissues starting as early as 2 hours p.i. The PA signals increased progressively, peaking at 10 to 12 hours and maintaining intensity for up to 72 hours. Conversely, PA signals from DrBphP alone became apparent within tumor tissues between 4 and 6 hours p.i. but diminished and disappeared by 8 hours. Notably, at the 10-hour imaging time point, DrBphP-CBD demonstrated stronger differential PA signals—approximately 7-fold (MDA-MB-231), 10.6-fold (MC38), and 2.5-fold (4T1) higher than those of DrBphP (Fig. 7C). These findings suggest that DrBphP-CBD exhibited an improved tumor-specific targeting and retention profile within the TME compared to DrBphP alone. The differential accumulation observed across various tumor models may be attributed to the distinct collagen expressions inherent to each tumor type. The MC38 and MDA-MB-231 tumors, characterized by their relatively high collagen content, exhibited a more substantial accumulation of DrBphP-CBD as opposed to the 4T1 tumors, which displayed a lower collagen density. This finding confirmed the sensitivity of the probe and its efficacy in tumors with variable collagen expression levels. The DrBphP-CBD–mediated differential PA imaging modality has proven effective in mitigating interference from nontargeted signals, such as those originating from tumor-associated vasculature, dermal layers, and
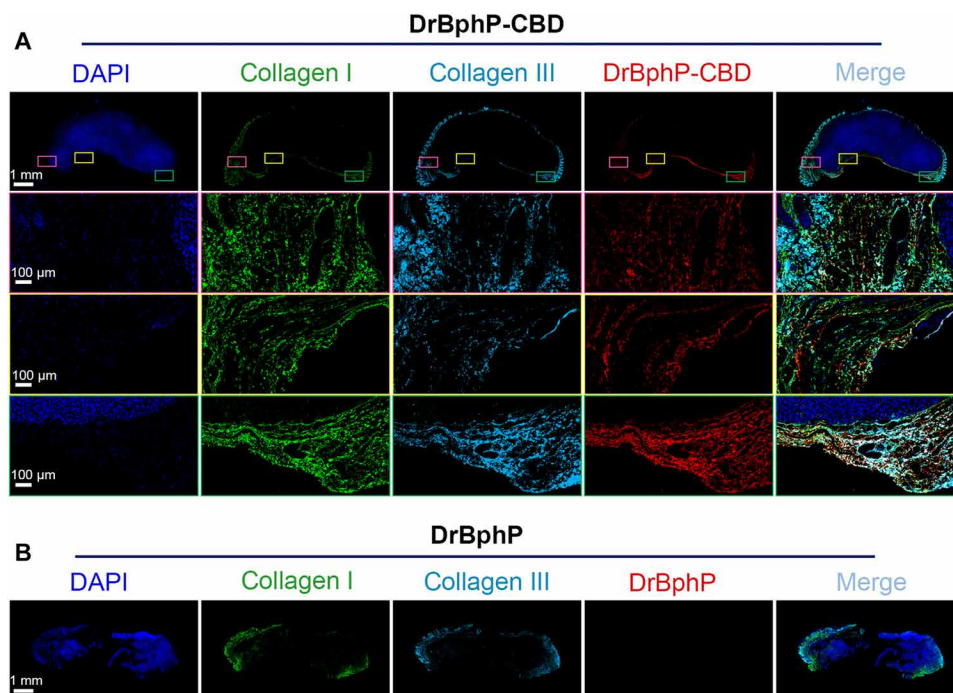
Fig. 4. Immunofluorescence images depicting MC38 tumor sections with binding of DrBphP-CBD or DrBphP. Sections are counterstained with 4′,6-diamidino-2-phenylindole (DAPI) for nuclear visualization. The top displays whole tumor views, while the bottom offers zoomed-in perspectives of the designated areas in the top, showcasing detailed binding interactions for DrBphP-CBD (**A**) and DrBphP (**B**).

melanin. This has resulted in the production of purified difference images. Time-course 3D PA imaging at 715 nm has also been demonstrated to achieve a high SNR and efficient imaging depth (*62*), which has facilitated the visualization of the intratumoral distribution of DrBphP-CBD (Fig. 7D and figs. S10 and S11). To better validate the targeted and enhanced imaging capabilities of DrBphP-CBD, we conducted additional experiments incorporating a nontargeted, nonphotoswitchable control. For this purpose, we used IR780, a lipophilic NIR dye known for its higher and more stable fluorescence intensity compared to the clinically used dye, indocyanine green. IR780 has been extensively evaluated as a PA imaging and photothermal agent in cancer theranostics (*63, 64*). We synthesized PEGylated IR780 NPs using a self-assembly method with distearoyl phosphatidyl ethanolamine-polyethylene glycol 2000 and IR780. As demonstrated in fig. S12 (A and B), these NPs exhibit strong absorption at 780 nm with an average particle size of 171 nm. In vitro assessments showed that the PA signal enhancement of the IR780 NPs was concentration dependent (fig. S12C). Subsequent in vivo PA images revealed that the PA signals of IR780 NPs became apparent within tumor tissues at 4 hours p.i., peaking at 6 hours (fig. S13A). However, the signals gradually decreased, likely due to the efflux of the IR780 NPs from tumor tissues, illustrating their limited tumor targeting and retention capabilities. Notably, the inability of IR780 NPs to undergo photoswitching resulted in a constant PA signal (fig. S13B), complicating differentiation from background signals, particularly in heterogeneous tumor tissues, and leading to potential inaccuracies in imaging and probe distribution analysis. In contrast, as illustrated in fig. S13C, PA signal switching dynamics for DrBphP-CBD showed that the

transition from ON to OFF state could be completed within 6 s during data collection at 760 nm. Following this, irradiation with a 635-nm laser for 10-s post-OFF state achieved full reversion to the ON state. DrBphP-CBD's photoswitchable nature markedly enhances imaging precision. The ability to switch DrBphP-CBD off provides a baseline measurement that can be subtracted from the ON state signal, considerably improving the SNR and yielding clearer, more precise images of probe distribution within tumors. This feature also facilitates real-time dynamic monitoring and precise quantitative analysis of probe concentrations and distributions, underlining the advantages of using photoswitchable probes in complex biological environments. These collective results highlighted the exceptional tumor targeting specificity, enhanced tumor retention, and heightened detection sensitivity of DrBphP-CBD.

Histological examinations were also performed to validate the PA signals of DrBphP-CBD. Tumor tissue specimens obtained at 10 hours p.i. of both DrBphP-CBD and DrBphP were subjected to PA imaging followed by histological analysis. As illustrated in Fig. 8, the presence of DrBphP-CBD was substantiated by the red fluorescence signal distribution. The localization of DrBphP-CBD within the stroma, in contrast to DrBphP, indicated a superior tumor retention. The differential PA images of multiple tumor results were in robust agreement with immunofluorescence images, both confirming the extensive tissue dispersion of DrBphP-CBD across tumor tissues and the precise PA localization facilitated by DrBphP-CBD. Furthermore, blood biochemistry analyses have indicated that both DrBphP-CBD and DrBphP groups exhibit good biocompatibility (figs. S14 and S15). Hematoxylin and eosin (H&E) staining performed on various organs of mice from both groups did not exhibit
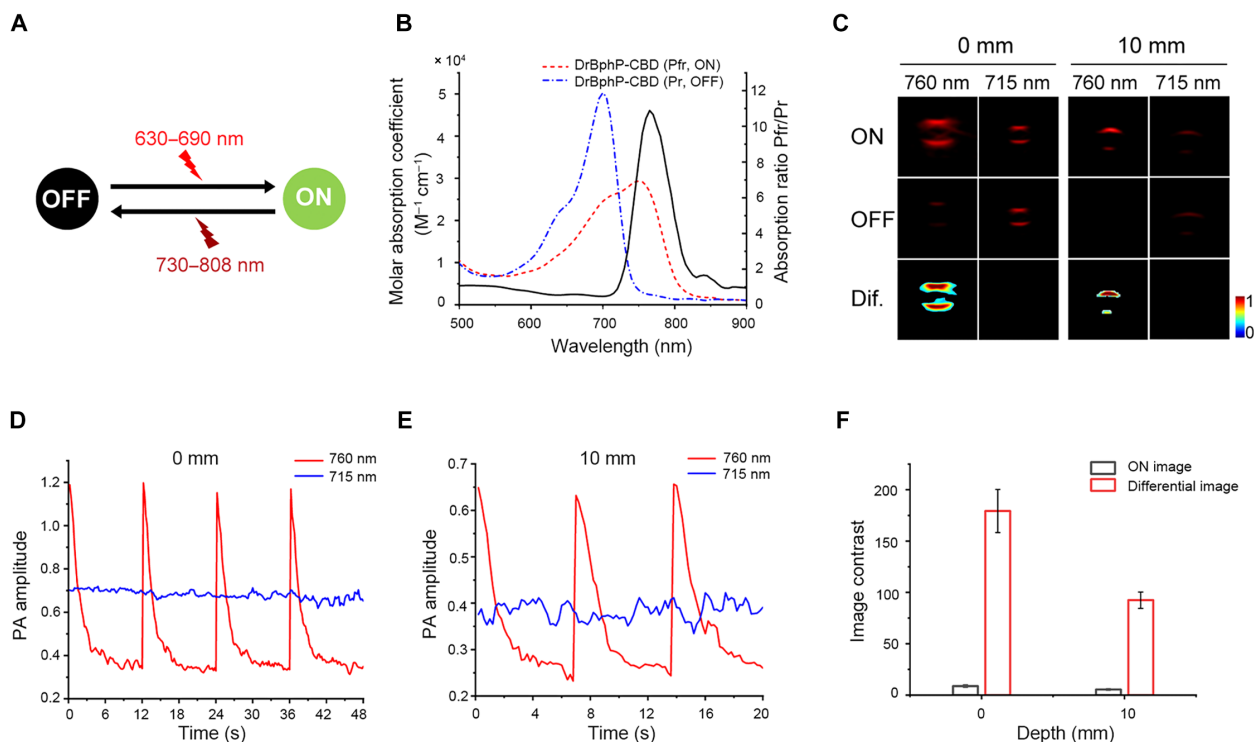
Fig. 5. Spectral and PA properties of DrBphP-CBD. (**A**) Photoswitching scheme of DrBphP-CBD induced by 730 to 808 nm (ON state, Pfr) and 630 to 690 nm (OFF state, Pr) light irradiation. (**B**) Molecular absorption spectra for DrBphP-CBD in ON and OFF states, featuring an absorption coefficient ratio (ON/OFF) of approximately 11 at 760 nm. (**C**) Representative PA images of DrBphP-CBD in water and within chicken breast tissue at 760 and 715 nm, delineating the ON and OFF states along with their differential response (Dif.). Reversible switching properties of DrBphP-CBD in water (**D**) and chicken breast tissue (**E**) under alternating light exposure. PA signal of DrBphP-CBD remains stable when exposed to 715-nm laser pulses. (**F**) Contrast analysis between ON and differential images at various tissue depths. Data are presented as mean ± SD ($n = 3$).

marked organ damage or inflammatory response (fig. S16). Together, these data confirmed that DrBphP-CBD can be used as an efficient and safe PA imaging contrast in cancer detection.

Overall, the innovative design and synthesis of DrBphP-CBD represent a stride in the realm of molecular imaging, providing a dual-functional tool for targeted, contrast-enhanced PA imaging of tumors. By ingeniously combining the photosensitive properties of DrBphP with the collagen-targeting capability of CBD, these protein assemblies efficiently home in on and adhere to the aberrant collagen expressed in neoplastic tissues (Fig. 9). The successful deployment of DrBphP-CBD in murine models has demonstrated their ability to offer heightened contrast and superior imaging specificity, effectively circumventing the challenges posed by endogenous absorption.

The fusion of DrBphP with CBD yields several advantages. First, leveraging a CBD derived from endogenous blood proteins reduces the likelihood of immune recognition. Second, these protein assemblies harness TME specificities—not by targeting a tumor-exclusive molecule but by exploiting unique tumor accessibility. In this regard, when compared with other tumor-targeting strategies like the use of engineered NPs or organic dyes, DrBphP-CBD assemblies offer an innovative approach by combining high specificity of targeting due to the collagen affinity with the robust stability and photoswitching capability of the BphPs. NPs may offer the advantage of passive accumulation within tumors via the EPR effect but often

lack such specific active targeting mechanisms and can exhibit variable intratumoral retention times. Similarly, organic dyes provide high contrast but may lack the targeted delivery and photostability that is intrinsic to DrBphP-CBD, which can be crucial for prolonged and repeat imaging required in clinical diagnostics. This approach circumvents potential clearance by endocytosis or the loss of binding sites due to mutations. Through intravenous delivery in various tumor models, DrBphP-CBD have exhibited increased tumor targeting and prolonged retention. This not only enhances the contrast-enhanced imaging of tumors but also reduces the background signal, thereby improving the diagnostic specificity of PA imaging. Such distinct photoswitching contrasts, coupled with the unique TME accessibility, allow DrBphP-CBD to serve as a universal platform for precise cancer detection and imaging.

While these findings validate the efficacy of DrBphP-CBD in enhancing imaging resolution and suggest their potential in clinical oncology diagnostics, there are several challenges to clinical translation that must be addressed. First, scaling up production remains a major hurdle. Achieving the high purity and batch consistency required for clinical use demands advanced manufacturing techniques and considerable investment. Second, regulatory considerations must be carefully navigated. The path from laboratory discovery to clinical trials involves rigorous scrutiny by regulatory bodies to ensure the safety and efficacy of the biologics, particularly in terms of tissue toxicity. Extensive toxicity studies must be undertaken to
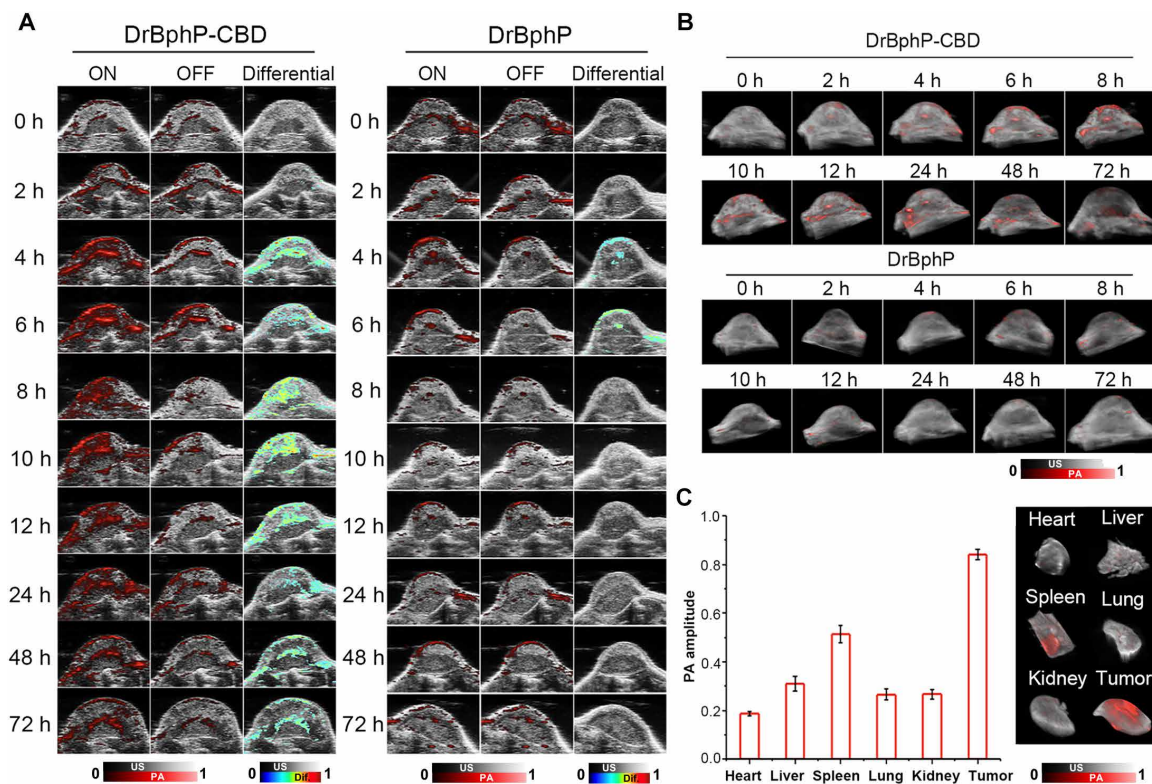
Fig. 6. Dynamic PA/US imaging postadministration of DrBphP-CBD in MC38 tumors. (**A**) Time-dependent PA/US images at 760 nm illustrating the ON state, OFF state, and their differential for both DrBphP-CBD and DrBphP. (**B**) 3D PA/US imaging at 715 nm, delineating the spatial distribution of DrBphP-CBD and DrBphP within tumors. (**C**) Ex vivo 3D PA/US imaging of various organs, tumor, and statistical quantification of PA signal amplitudes. Data are presented as mean $\pm$ SD ($n = 3$).

confirm that the integration of DrBphP with CBD does not elicit adverse effects in human tissues.

Furthermore, our study has limitations that future research should aim to overcome. For instance, while the protein assemblies exhibit increased tumor targeting and prolonged retention, their long-term stability and potential immunogenicity in humans remain to be thoroughly evaluated. In addition, the reliance on murine models may not fully predict human outcomes. Future strategies should include the development of more sophisticated animal models that more closely mimic human tumor biology or the use of organoid systems.

Our work illustrates the profound impact of engineered protein assemblies on the spatial and temporal resolution of bioimaging. By refining the sensitivity and specificity of PA imaging, DrBphP-CBD hold the promise to greatly advance early cancer detection, provide invaluable guidance during surgical interventions, and contribute to the meticulous monitoring of disease progression. This work exemplifies the confluence of innovative NP engineering and precision medicine. Moving forward, our approach must evolve to address these complex challenges, paving the way toward the practical clinical application of these innovative imaging tools in precision medicine.

MATERIALS AND METHODS
Protein expression and purification
The DrBphP-CBD gene was codon-optimized for *E. coli* expression by GenScript and subsequently polymerase chain reaction–amplified.

The amplified product was subcloned into the pET28a vector (GE Healthcare, USA), using the Nde I and Xho I restriction sites. This vector confers an N-terminal His6 tag to facilitate subsequent purification steps. Expression of the recombinant DrBphP-CBD protein was induced in bacterial cultures at an optical density of 600 nm of 0.8, using 0.8 mM isopropyl-β-D-thiogalactopyranoside (Sigma-Aldrich). Following induction, the cultures were incubated at 16°C for 20 hours. Cell harvest was achieved through centrifugation at 8000 rpm for 30 min, and the pellet was resuspended in a binding buffer composed of 30 mM tris-HCl (pH 7.6), 500 mM NaCl, 5 mM imidazole, 0.1 mM BV hydrochloride (Sigma-Aldrich), 1 mM tris (2-carboxyethyl) phosphine hydrochloride (Sigma-Aldrich), and 0.5 mM protease inhibitor phenylmethylsulfonyl fluoride (Sigma-Aldrich). Cell lysis was performed using an ultrahigh-pressure homogenizer (AH-NANO, ATS, China), and the clarified lysate was obtained by centrifugation at 20,000 rpm for 50 min. The supernatant was then subjected to IMAC using HisTrap HP columns (Cytiva, USA) on an AKTA Pure FPLC system (Cytiva, USA). The protein fractions eluted from IMAC were pooled and further purified by SEC on a Superdex 200 16/600 column (Cytiva, USA). The homogeneity of the purified DrBphP-CBD protein was confirmed by SDS-PAGE analysis, and the protein was lyophilized and stored at −80°C for application.

Protein modeling
Protein structural elucidation was achieved through computational modeling using AlphaFold-Multimer (*58*), an advanced iteration of
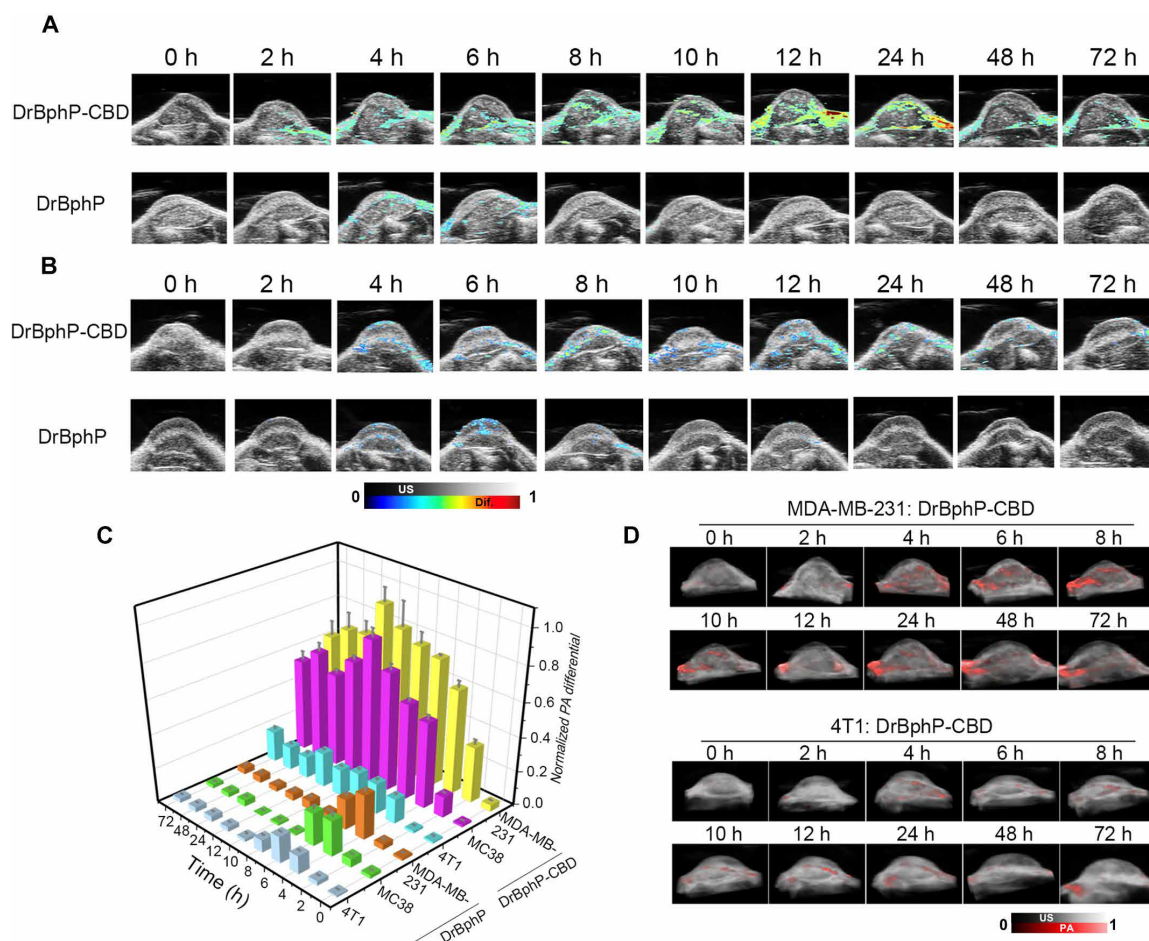
Fig. 7. Time-resolved PA/US images of different tumor models treated with DrBphP-CBD. (**A** and **B**) Differential PA images of MDA-MB-231 (A) and 4T1 (B) tumor-bearing mice captured over various time intervals before and following the intravenous administration of DrBphP-CBD or DrBphP (0.9 µmol/kg). (**C**) Quantitative evaluation of differential PA amplitudes at 760 nm in multiple tumors following intravenous injection of DrBphP-CBD or DrBphP (0.9 µmol/kg). (**D**) 3D PA/US images at 715 nm of DrBphP-CBD in MDA-MB-231 and 4T1 tumors, measured at different time points.

the AlphaFold2 algorithm. Specifically, computational predictions were focused on the dimerization domain of DrBphP (Q9RZA4, residues 1 to 594), the trimerization domain of CBD (P04275, residues 1683 to 1873), and the interaction between CBD and type I collagen. The iterative modeling process comprised up to 24 cycles, avoiding the reliance on template structures. Subsequent energy refinement was performed using the AMBER force field within the ColabFold environment, adhering to the standard protocols. Multiple sequence alignments were generated via MMseqs2, and structural congruity was evaluated using the TM score metric as provided by Foldseek. This metric, which normalizes for the length of the reference protein, quantifies structural correspondence on a scale from 0 to 1, where 1 signifies perfect congruence. Scores exceeding 0.5 are indicative of high fidelity in model prediction, whereas scores below 0.17 suggest nonsubstantial similarity, potentially attributable to chance. In our analyses, the dimerization and trimerization structures of DrBphP and CBD attained TM scores of 0.835 and 0.539, respectively, and the complex structure of CBD and type I collagen attained TM scores of 0.842, reflecting a high degree of confidence in the structural predictions made by AlphaFold2 (*57*). For visualization

and further structural analyses, the predicted models were rendered using the PyMOL software suite (https://pymol.org).

Binding affinity assay
ELISA plates were coated with collagen I or collagen III [10 µg/ml each in phosphate-buffered saline (PBS)] overnight at 37°C, blocked with 2% bovine serum albumin in PBS with 0.05% Tween 20 (PBS-T) for 1 hour at room temperature, and washed. DrBphP-CBD was then added in increasing concentrations for 2 hours. Following washes with PBS-T, plates were incubated with anti-His antibody (ab18184, Abcam) and goat anti-mouse horseradish peroxidase–conjugated antibody (ab205719, Abcam). Detection was performed using tetramethylbenzidine substrate, and the equilibrium K_d were calculated using Prism software based on one site–specific binding.

Physical characterization
Hydrodynamic size measurements were conducted with a Malvern Nano-zetasizer. Ultraviolet-visible (UV-vis) spectra were obtained using an Agilent Cary 60 UV-vis spectrophotometer. TEM images were captured with an HT7700 microscope (Hitachi Ltd., Japan),
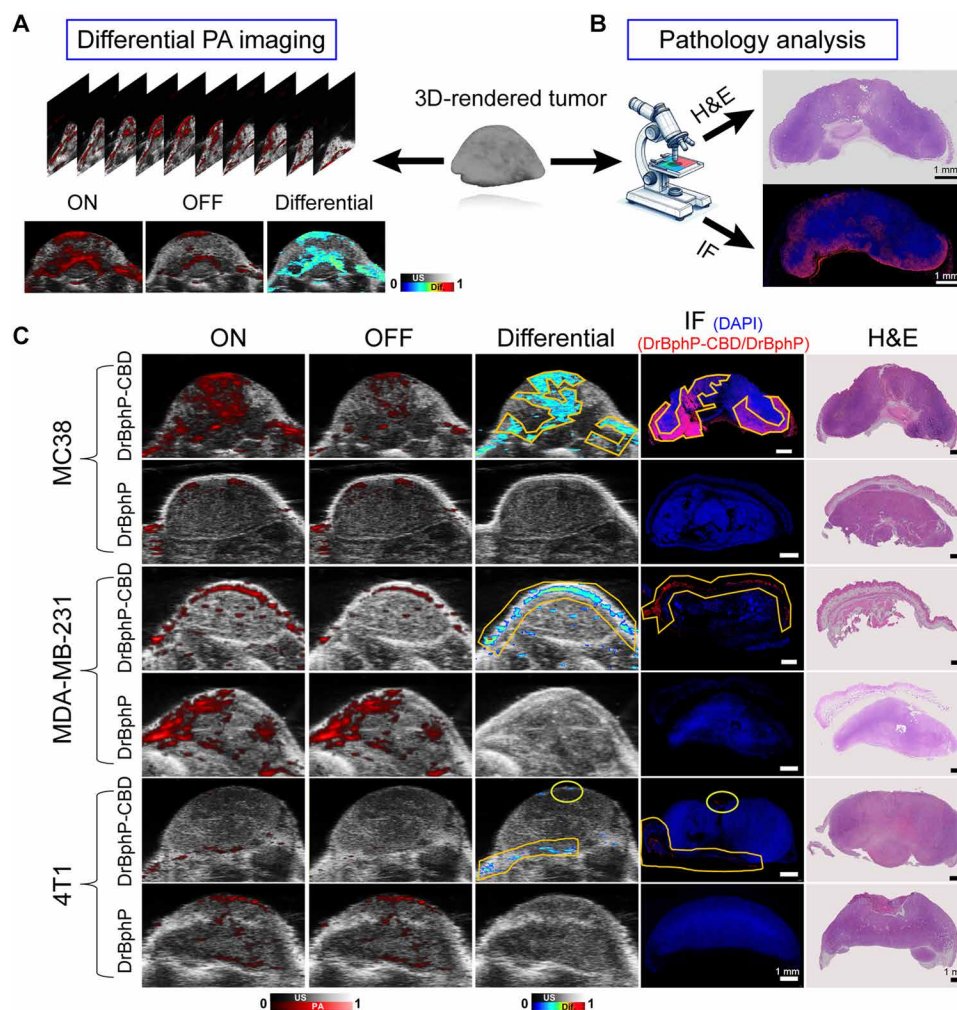
Fig. 8. Comparative analysis of contrast-enhanced PA imaging and immunofluorescence in tumor tissue specimens. (**A**) Utilization of DrBphP-CBD for enhanced differential PA images of tumors. (**B**) Histopathological examination images of entire tumor tissue specimens. (**C**) Correlation of representative differential PA images with corresponding immunofluorescence (IF) and H&E images. Scale bars, 1 mm.

and AFM images were captured with a Multimode VIII (Bruker, Germany) in tapping mode using hard silicon cantilevers (spring constant, 40 N/m).

Tumor mouse model
Female BALB/C nude mice aged 4 to 6 weeks were acquired from Guangdong Medicinal Laboratory Animal Center (Guangzhou, China) and handled following the regulations of the Animal Ethical and Welfare Committee of Shenzhen University. Mice were kept under controlled conditions (22°C, 40 to 70% humidity, 12-hour light-dark cycles) with sterile food and water. Subcutaneous injections into the right hindlimb included MC38 cells (3×10^6 cell per site) in RPMI 1640 serum-free medium, 4T1 cells (1×10^6 cell per site), and MDA-MB-231 cells (6×10^6 cell per site) in Dulbecco's modified Eagle's medium serum-free medium supplemented with Corning Matrigel matrix to support tumor establishment.

Intravital microscopy
Intravital microscopy was conducted using a two-photon laser scanning microscopy system (IVM-MS2, IVIM Technology). Murine models with established MC38, MDA-MB-231, and 4T1 tumors ($n = 3$) received intravenous injections of DrBphP-CBD or DrBphP solutions (dose of 0.9 μmol/kg). The acquisition of SHG imaging, along with fluorescence signals attributable to DrBphP-CBD or DrBphP at specified emission wavelengths, was performed at the tumor sites. These measurements were systematically recorded at pre-established temporal intervals (0, 2, 4, 6, 8, 10, 12, 24, 48, and 72 hours p.i.) to facilitate the dynamic visualization of the TME and the precise localization of DrBphP-CBD or DrBphP. Throughout the imaging procedure, the thermal homeostasis of each subject was rigorously maintained at a physiological temperature of 37°C via a dedicated homeothermic blanket system (RightTemp, Kent Scientific), thereby ensuring normothermic conditions.

PA imaging
PA imaging in vitro was executed using the Visualsonics LAZR-X Vevo system (Fujifilm, Japan) equipped with a 256-element transducer array (MX550D, 25 to 55 MHz) and a nanosecond pulsed laser (pulse width of 10 ns and repetition frequency of 20 Hz). Solutions of DrBphP-CBD or DrBphP (0.2 mM) were enclosed within
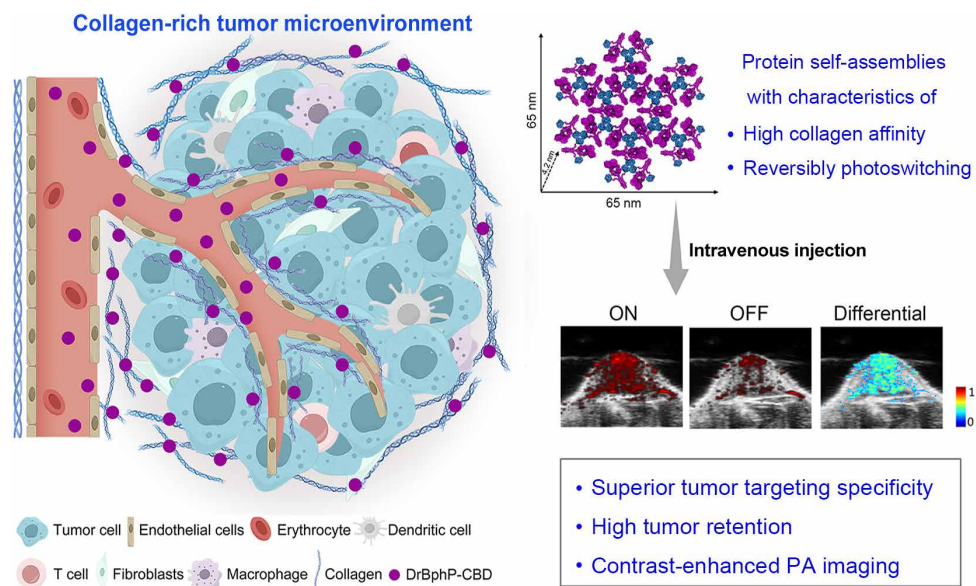
Fig. 9. Schematic illustration of design and application of DrBphP-CBD assemblies. Engineered DrBphP-CBD self-assemblies with collagen binding affinity and reversibly photoswitching capability enhance tumor PA imaging specificity and contrast.

transparent polyurethane tubing and submerged in a water tank for acoustic coupling. Photoactivation of DrBphP-CBD or DrBphP to their Pr and Pfr states was induced under 635- and 808-nm laser irradiation.

In vivo PA imaging was performed according to the previous study (62), and murine models with tumors were anesthetized using 2% isoflurane carried in oxygen through a nose cone, with thermoregulation maintained via a heating pad. Sequential PA images were acquired at baseline and at intervals postintravenous administration of DrBphP-CBD, DrBphP (at a dose of 0.9 µmol/kg), and IR780 NPs (4 mg/kg). The 3D PA mode at 715 nm of the Vevo LAZR-X system was used to capture the corresponding signals. Photostimulation of DrBphP-CBD or DrBphP was conducted using 760-nm light, while 635-nm light was used for protein activation.

For biodistribution analysis, tumor-bearing mice ($n = 3$) received intravenous injections of DrBphP-CBD or DrBphP. At 10 hours following administration, the mice were humanely euthanized, and the tumors along with principal organs—heart, lungs, liver, spleen, and kidneys—were excised. The Vevo LAZR-X system was then used to detect and reconstruct a 3D PA signal model of these tissues, thereby facilitating a comprehensive visualization of the compounds' biodistribution.

In vitro hemolysis assay
Fresh blood was harvested from female BALB/c nude mice, subjected to centrifugation at 380g to separate red blood cells (RBCs), which were then resuspended appropriately. Various concentrations of DrBphP-CBD or DrBphP solutions (200 µl) were administered to 1 ml of the RBC suspension and were then incubated at room temperature for 4 hours. For controls, RBC suspensions were incubated with water as the positive control and with PBS as the negative control. Following incubation, centrifugation at 13,500g facilitated the separation of the supernatant, the optical density of which was

ascertained at a wavelength of 540 nm via a microplate reader. The percentage of hemolysis was quantified using the formula: hemolysis (%) = [(absorbance of the sample − absorbance of the PBS control)/ (absorbance of the water control − absorbance of the PBS)] × 100%.

In vivo biocompatibility examination
For long-term biocompatibility, blood samples and major organs (heart, spleen, kidney, liver, lung, and muscle) were collected from mice after 7 days. Blood samples were used for complete blood panel analysis and serum biochemistry test. The organs were fixed in 4% paraformaldehyde and stained with H&E for histological analysis.

Histological studies and immunofluorescence
Tumors were fixed, paraffin-embedded, and sectioned for H&E staining (G1005, Servicebio). Specific anti–collagen I (catalog no. GB11022-3-100, Servicebio), anti–collagen III (catalog no. GB111629-100, Servicebio), and anti-His monoclonal antibody (ab18184, Abcam) were used for additional staining. Imaging was done using a Virtual slide microscope (Olympus VS120, Japan) and a confocal laser scanning microscope (Zeiss LSM 710) for immunofluorescence.

Statistical analysis
In this study, experimental results were reported as mean ± SD ($n \geq 3$). Quantitative analysis of immunofluorescence intensities within tumors was conducted using ImageJ software. Statistical analysis was performed using Origin 2021 or GraphPad Prism 8.0 software.

Supplementary Materials
This PDF file includes:
Figs. S1 to S16

REFERENCES AND NOTES

1. L. V. Wang, J. Yao, A practical guide to photoacoustic tomography in the life sciences. *Nat. Methods* **13**, 627–638 (2016).
2. L. V. Wang, S. Hu, Photoacoustic tomography: In vivo imaging from organelles to organs. *Science* **335**, 1458–1462 (2012).
3. X. Wang, Y. Pang, G. Ku, X. Xie, G. Stoica, L. V. Wang, Noninvasive laser-induced photoacoustic tomography for structural and functional in vivo imaging of the brain. *Nat. Biotechnol.* **21**, 803–806 (2003).
4. S. Wang, J. Lin, T. Wang, X. Chen, P. Huang, Recent advances in photoacoustic imaging for deep-tissue biomedical applications. *Theranostics* **6**, 2394–2413 (2016).
5. J. Weber, P. C. Beard, S. E. Bohndiek, Contrast agents for molecular photoacoustic imaging. *Nat. Methods* **13**, 639–650 (2016).
6. Q. Fu, R. Zhu, J. Song, H. Yang, X. Chen, Photoacoustic imaging: Contrast agents and their biomedical applications. *Adv. Mater.* **31**, 1805875 (2019).
7. J. Mu, M. Xiao, Y. Shi, X. Geng, H. Li, Y. Yin, X. Chen, The chemistry of organic contrast agents in the NIR-II window. *Angew. Chem. Int. Ed. Engl.* **61**, e202114722 (2022).
8. C. Xu, J. Huang, Y. Jiang, S. He, C. Zhang, K. Pu, Nanoparticles with ultrasound-induced afterglow luminescence for tumour-specific theranostics. *Nat. Biomed. Eng.* **7**, 298–312 (2023).
9. Y. Ren, A. C. Sedgwick, J. Chen, G. Thiabaud, C. V. Chau, J. An, J. F. Arambula, X.-P. He, J. S. Kim, J. L. Sessler, C. Liu, Manganese (II) Texaphyrin: A paramagnetic photoacoustic contrast agent activated by near-IR light. *J. Am. Chem. Soc.* **142**, 16156–16160 (2020).
10. L. Zeng, G. Ma, J. Lin, P. Huang, Photoacoustic probes for molecular detection: Recent advances and perspectives. *Small* **14**, 1800782 (2018).
11. J. Yao, A. A. Kaberniuk, L. Li, D. M. Shcherbakova, R. Zhang, L. Wang, G. Li, V. V. Verkhusha, L. V. Wang, Multiscale photoacoustic tomography using reversibly switchable bacterial phytochrome as a near-infrared photochromic probe. *Nat. Methods* **13**, 67–73 (2016).
12. L. Li, A. A. Shemetov, M. Baloban, P. Hu, L. Zhu, D. M. Shcherbakova, R. Zhang, J. Shi, J. Yao, L. V. Wang, Small near-infrared photochromic protein for photoacoustic multi-contrast imaging and detection of protein interactions in vivo. *Nat. Commun.* **9**, 2734 (2018).
13. J. Yang, L. Li, A. A. Shemetov, S. Lee, Y. Zhao, Y. Liu, Y. Shen, J. Li, Y. Oka, V. V. Verkhusha, L. V. Wang, Focusing light inside live tissue using reversibly switchable bacterial phytochrome as a genetically encoded photochromic guide star. *Sci. Adv.* **5**, eaay1211 (2019).
14. K. Mishra, M. Stankevych, J. P. Fuenzalida-Werner, S. Grassmann, V. Gujrati, Y. Huang, U. Klemm, V. R. Buchholz, V. Ntziachristos, A. C. Stiel, Multiplexed whole-animal imaging with reversibly switchable optoacoustic proteins. *Sci. Adv.* **6**, eaaz6293 (2020).
15. R. Gao, F. Liu, W. Liu, S. Zeng, J. Chen, R. Gao, L. Wang, C. Fang, L. Song, A. C. Sedgwick, J. L. Sessler, J. Chu, F. Yan, C. Liu, Background-suppressed tumor-targeted photoacoustic imaging using bacterial carriers. *Proc. Natl. Acad. Sci. U.S.A.* **119**, e2121982119 (2022).
16. L. A. Kasatkina, C. Ma, M. E. Matlashov, T. Vu, M. Li, A. A. Kaberniuk, J. Yao, V. V. Verkhusha, Optogenetic manipulation and photoacoustic imaging using a near-infrared transgenic mouse model. *Nat. Commun.* **13**, 2813 (2022).
17. Y. Kuwasaki, K. Suzuki, G. Yu, S. Yamamoto, T. Otabe, Y. Kakihara, M. Nishiwaki, K. Miyake, K. Fushimi, R. Bekdash, Y. Shimizu, R. Narikawa, T. Nakajima, M. Yazawa, M. Sato, A red light–responsive photoswitch for deep tissue optogenetics. *Nat. Biotechnol.* **40**, 1672–1679 (2022).
18. W. Y. Wahlgren, E. Claesson, I. Tuure, S. Trillo-Muyo, S. Bódizs, J. A. Ihalainen, H. Takala, S. Westenhoff, Structural mechanism of signal transduction in a phytochrome histidine kinase. *Nat. Commun.* **13**, 7673 (2022).
19. L. H. Otero, S. Foscaldi, G. T. Antelo, G. L. Rosano, S. Sirigu, S. Klinke, L. A. Defelipe, M. Sánchez-Lamas, G. Battocchio, V. Conforte, A. A. Vojnov, L. M. G. Chavas, F. A. Goldbaum, M.-A. Mroginski, J. Rinaldi, H. R. Bonomi, Structural basis for the Pr-Pfr long-range signaling mechanism of a full-length bacterial phytochrome at the atomic level. *Sci. Adv.* **7**, eabh1097 (2021).
20. R. K. Chee, Y. Li, W. Zhang, R. E. Campbell, R. J. Zemp, In vivo photoacoustic difference-spectra imaging of bacteria using photoswitchable chromoproteins. *J. Biomed. Opt.* **23**, 106006 (2018).
21. M. S. Lee, D. W. Yee, M. Ye, R. J. Macfarlane, Nanoparticle assembly as a materials development tool. *J. Am. Chem. Soc.* **144**, 3330–3346 (2022).
22. J. Ouyang, A. Xie, J. Zhou, R. Liu, L. Wang, H. Liu, N. Kong, W. Tao, Minimally invasive nanomedicine: Nanotechnology in photo−/ultrasound−/radiation−/magnetism-mediated therapy and imaging. *Chem. Soc. Rev.* **51**, 4996–5041 (2022).
23. J. Chen, J. Qi, C. Chen, J. Chen, L. Liu, R. Gao, T. Zhang, L. Song, D. Ding, P. Zhang, C. Liu, Tocilizumab–Conjugated Polymer Nanoparticles for NIR-II Photoacoustic-Imaging-Guided Therapy of Rheumatoid Arthritis. *Adv. Mater.* **32**, 2003399 (2020).
24. P. Cheng, W. Chen, S. Li, S. He, Q. Miao, K. Pu, Fluoro-photoacoustic polymeric renal reporter for real-time dual imaging of acute kidney injury. *Adv. Mater.* **32**, 1908530 (2020).
25. G. He, Y. Li, M. R. Younis, L.-H. Fu, T. He, S. Lei, J. Lin, P. Huang, Synthetic biology-instructed transdermal microneedle patch for traceable photodynamic therapy. *Nat. Commun.* **13**, 6238 (2022).
26. H. Chen, W. Zhang, G. Zhu, J. Xie, X. Chen, Rethinking cancer nanotheranostics. *Nat. Rev. Mater.* **2**, 17024 (2017).
27. Y. Li, J. A. Champion, Self-assembling nanocarriers from engineered proteins: Design, functionalization, and application for drug delivery. *Adv. Drug Deliv. Rev.* **189**, 114462 (2022).
28. L. He, X. Lin, Y. Wang, C. Abraham, C. Sou, T. Ngo, Y. Zhang, I. A. Wilson, J. Zhu, Single-component, self-assembling, protein nanoparticles presenting the receptor binding domain and stabilized spike as SARS-CoV-2 vaccine candidates. *Sci. Adv.* **7**, eabf1591 (2021).
29. Y.-N. Zhang, J. Paynter, A. Antanasijevic, J. D. Allen, M. Eldad, Y.-Z. Lee, J. Copps, M. L. Newby, L. He, D. Chavez, P. Frost, A. Goodroe, J. Dutton, R. Lanford, C. Chen, I. A. Wilson, M. Crispin, A. B. Ward, J. Zhu, Single-component multilayered self-assembling protein nanoparticles presenting glycan-trimmed uncleaved prefusion optimized envelope trimers as HIV-1 vaccine candidates. *Nat. Commun.* **14**, 1985 (2023).
30. L. He, A. Chaudhary, X. Lin, C. Sou, T. Alkutkar, S. Kumar, T. Ngo, E. Kosviner, G. Ozorowski, R. L. Stanfield, A. B. Ward, I. A. Wilson, J. Zhu, Single-component multilayered self-assembling nanoparticles presenting rationally designed glycoprotein trimers as Ebola virus vaccines. *Nat. Commun.* **12**, 2633 (2021).
31. W.-S. Kim, S. Min, S. K. Kim, S. Kang, S. An, E. Criado-Hidalgo, H. Davis, A. Bar-Zion, D. Malounda, Y. H. Kim, J.-H. Lee, S. H. Bae, J. G. Lee, M. Kwak, S.-W. Cho, M. G. Shapiro, J. Cheon, Magneto-acoustic protein nanostructures for non-invasive imaging of tissue mechanics in vivo. *Nat. Mater.* **23**, 290–300 (2024).
32. K. Ling, H. Wu, A. S. Neish, J. A. Champion, Alginate/chitosan microparticles for gastric passage and intestinal release of therapeutic protein nanoparticles. *J. Control. Release* **295**, 174–186 (2019).
33. J. F. Ross, G. C. Wildsmith, M. Johnson, D. L. Hurdiss, K. Hollingsworth, R. F. Thompson, M. Mosayebi, C. H. Trinh, E. Paci, A. R. Pearson, M. E. Webb, W. B. Turnbull, Directed assembly of homopentameric cholera toxin B-subunit proteins into higher-order structures using coiled-coil appendages. *J. Am. Chem. Soc.* **141**, 5211–5219 (2019).
34. J. Marcandalli, B. Fiala, S. Ols, M. Perotti, W. de van der Schueren, J. Snijder, E. Hodge, M. Benhaim, R. Ravichandran, L. Carter, W. Sheffler, L. Brunner, M. Lawrenz, P. Dubois, A. Lanzavecchia, F. Sallusto, K. K. Lee, D. Veesler, C. E. Correnti, L. J. Stewart, D. Baker, K. Loré, L. Perez, N. P. King, Induction of potent neutralizing antibody responses by a designed protein nanoparticle vaccine for respiratory syncytial virus. *Cell* **176**, 1420–1431.e17 (2019).
35. A. Ljubetič, F. Lapenta, H. Gradišar, I. Drobnak, J. Aupič, Ž. Strmšek, D. Lainšček, I. Hafner-Bratkovič, A. Majerle, N. Krivec, M. Benčina, T. Pisanski, T. Ć. Veličković, A. Round, J. M. Carazo, R. Melero, R. Jerala, Design of coiled-coil protein-origami cages that self-assemble in vitro and in vivo. *Nat. Biotechnol.* **35**, 1094–1101 (2017).
36. D. R. Dautel, J. A. Champion, Protein vesicles self-assembled from functional globular proteins with different charge and size. *Biomacromolecules* **22**, 116–125 (2021).
37. D. Diaz, A. Care, A. Sunna, Bioengineering strategies for protein-based nanoparticles. *Genes* **9**, 370 (2018).
38. I. Kalvet, M. Ortmayer, J. Zhao, R. Crawshaw, N. M. Ennist, C. Levy, A. Roy, A. P. Green, D. Baker, Design of heme enzymes with a tunable substrate binding pocket adjacent to an open metal coordination site. *J. Am. Chem. Soc.* **145**, 14307–14315 (2023).
39. M. G. Shapiro, P. W. Goodwill, A. Neogy, M. Yin, F. S. Foster, D. V. Schaffer, S. M. Conolly, Biogenic gas nanostructures as ultrasonic molecular reporters. *Nat. Nanotechnol.* **9**, 311–316 (2014).
40. A. Schmidt, L. Sauthof, M. Szczepek, M. F. Lopez, F. V. Escobar, B. M. Qureshi, N. Michael, D. Buhrke, T. Stevens, D. Kwiatkowski, D. von Stetten, M. A. Mroginski, N. Krauß, T. Lamparter, P. Hildebrandt, P. Scheerer, Structural snapshot of a bacterial phytochrome in its functional intermediate state. *Nat. Commun.* **9**, 4912 (2018).
41. C. Dubois, L. Panicot-Dubois, G. Merrill-Skoloff, B. Furie, B. C. Furie, Glycoprotein VI–dependent and–independent pathways of thrombus formation in vivo. *Blood* **107**, 3902–3906 (2006).
42. H. Liang, X. Li, B. Chen, B. Wang, Y. Zhao, Y. Zhuang, H. Shen, Z. Zhang, J. Dai, A collagen-binding EGFR single-chain Fv antibody fragment for the targeted cancer therapy. *J. Control. Release* **209**, 101–109 (2015).
43. J. Riegler, Y. Labyed, S. Rosenzweig, V. Javinal, A. Castiglioni, C. X. Dominguez, J. E. Long, Q. Li, W. Sandoval, M. R. Junttila, S. J. Turley, J. Schartner, R. A. D. Carano, Tumor elastography and its association with collagen and the tumor microenvironment. *Clin. Cancer Res.* **24**, 4455–4467 (2018).
44. J. Ishihara, A. Ishihara, K. Sasaki, S. S.-Y. Lee, J.-M. Williford, M. Yasui, H. Abe, L. Potin, P. Hosseinchi, K. Fukunaga, M. M. Raczy, L. T. Gray, A. Mansurov, K. Katsumata, M. Fukayama, S. J. Kron, M. A. Swartz, J. A. Hubbell, Targeted antibody and cytokine cancer immunotherapies through collagen affinity. *Sci. Transl. Med.* **11**, eaau3259 (2019).
45. A. Mansurov, J. Ishihara, P. Hosseinchi, L. Potin, T. M. Marchell, A. Ishihara, J.-M. Williford, A. T. Alpar, M. M. Raczy, L. T. Gray, M. A. Swartz, J. A. Hubbell, Collagen-binding IL-12 enhances tumour inflammation and drives the complete remission of established immunologically cold mouse tumours. *Nat. Biomed. Eng.* **4**, 531–543 (2020).

46. N. Momin, N. K. Mehta, N. R. Bennett, L. Ma, J. R. Palmeri, M. M. Chinn, E. A. Lutz, B. Kang, D. J. Irvine, S. Spranger, K. D. Wittrup, Anchoring of intratumorally administered cytokines to collagen safely potentiates systemic cancer immunotherapy. *Sci. Transl. Med.* **11**, eaaw2614 (2019).

47. N. Momin, J. R. Palmeri, E. A. Lutz, N. Jailkhani, H. Mak, A. Tabet, M. M. Chinn, B. H. Kang, V. Spanoudaki, R. O. Hynes, K. D. Wittrup, Maximizing response to intratumoral immunotherapy in mice by tuning local retention. *Nat. Commun.* **13**, 109 (2022).

48. Y. Li, Z. Su, W. Zhao, X. Zhang, N. Momin, C. Zhang, K. D. Wittrup, Y. Dong, D. J. Irvine, R. Weiss, Multifunctional oncolytic nanoparticles deliver self-replicating IL-12 RNA to eliminate established tumors and prime systemic immunity. *Nat. Cancer* **1**, 882–893 (2020).

49. A. B. Silver, S. Y. Tzeng, M. Lager, J. Wang, J. Ishihara, J. J. Green, J. B. Spangler, An engineered immunocytokine with collagen affinity improves the tumor bioavailability, tolerability, and therapeutic efficacy of IL-2. *Cell Rep. Med.* **4**, 101289 (2023).

50. J. A. Stinson, A. Sheen, N. Momin, J. Hampel, R. Bernstein, R. Kamerer, B. Fadl-Alla, J. Samuelson, E. Fink, T. M. Fan, K. D. Wittrup, Collagen-anchored interleukin-2 and interleukin-12 safely reprogram the tumor microenvironment in canine soft-tissue sarcomas. *Clin. Cancer Res.* **29**, 2110–2122 (2023).

51. S. Kang, A. Mansurov, T. Kurtanich, H. R. Chun, A. J. Slezak, L. R. Volpatti, K. Chang, T. Wang, A. T. Alpar, K. C. Refvik, O. I. Hansen, G. J. Borjas, H.-N. Shim, K. T. Hultgren, S. Gomes, A. Solanki, J. Ishihara, M. A. Swartz, J. A. Hubbell, Engineered IL-7 synergizes with IL-12 immunotherapy to prevent T cell exhaustion and promote memory without exacerbating toxicity. *Sci. Adv.* **9**, eadh9879 (2023).

52. J.-M. Williford, J. Ishihara, A. Ishihara, A. Mansurov, P. Hosseinchi, T. M. Marchell, L. Potin, M. A. Swartz, J. A. Hubbell, Recruitment of CD103+ dendritic cells via tumor-targeted chemokine delivery enhances efficacy of checkpoint inhibitor immunotherapy. *Sci. Adv.* **5**, eaay1357 (2019).

53. K. Sasaki, J. Ishihara, A. Ishihara, R. Miura, A. Mansurov, K. Fukunaga, J. A. Hubbell, Engineered collagen-binding serum albumin as a drug conjugate carrier for cancer therapy. *Sci. Adv.* **5**, eaaw6081 (2019).

54. H. Cabral, Y. Matsumoto, K. Mizuno, Q. Chen, M. Murakami, M. Kimura, Y. Terada, M. R. Kano, K. Miyazono, M. Uesaka, N. Nishiyama, K. Kataoka, Accumulation of sub-100 nm polymeric micelles in poorly permeable tumours depends on size. *Nat. Nanotechnol.* **6**, 815–823 (2011).

55. Y. Bai, Q. Luo, J. Liu, Protein self-assembly via supramolecular strategies. *Chem. Soc. Rev.* **45**, 2756–2767 (2016).

56. J. E. Padilla, C. Colovos, T. O. Yeates, Nanohedra: Using symmetry to design self assembling protein cages, layers, crystals, and filaments. *Proc. Natl. Acad. Sci. U.S.A.* **98**, 2217–2221 (2001).

57. K. Tunyasuvunakool, J. Adler, Z. Wu, T. Green, M. Zielinski, A. Žídek, A. Bridgland, A. Cowie, C. Meyer, A. Laydon, S. Velankar, G. J. Kleywegt, A. Bateman, R. Evans, A. Pritzel, M. Figurnov, O. Ronneberger, R. Bates, S. A. A. Kohl, A. Potapenko, A. J. Ballard, B. Romera-Paredes, S. Nikolov, R. Jain, E. Clancy, D. Reiman, S. Petersen, A. W. Senior, K. Kavukcuoglu, E. Birney, P. Kohli, J. Jumper, D. Hassabis, Highly accurate protein structure prediction for the human proteome. *Nature* **596**, 590–596 (2021).

58. R. Evans, M. O'Neill, A. Pritzel, N. Antropova, A. Senior, T. Green, A. Žídek, R. Bates, S. Blackwell, J. Yim, O. Ronneberger, S. Bodenstein, M. Zielinski, A. Bridgland, A. Potapenko, A. Cowie, K. Tunyasuvunakool, R. Jain, E. Clancy, P. Kohli, J. Jumper, D. Hassabis, Protein complex prediction with AlphaFold-Multimer. bioRxiv 463034 [Preprint] (2022). https://doi.org/10.1101/2021.10.04.463034.

59. T. H. C. Brondijk, D. Bihan, R. W. Farndale, E. G. Huizinga, Implications for collagen I chain registry from the structure of the collagen von Willebrand factor A3 domain complex. *Proc. Natl. Acad. Sci. U.S.A.* **109**, 5253–5258 (2012).

60. E. Brown, T. McKee, E. diTomaso, A. Pluen, B. Seed, Y. Boucher, R. K. Jain, Dynamic imaging of collagen and its modulation in tumors in vivo using second-harmonic generation. *Nat. Med.* **9**, 796–800 (2003).

61. X. Chen, O. Nadiarynkh, S. Plotnikov, P. J. Campagnola, Second harmonic generation microscopy for quantitative analysis of collagen fibrillar structure. *Nat. Protoc.* **7**, 654–669 (2012).

62. S. Lei, J. Zhang, N. T. Blum, M. Li, D.-Y. Zhang, W. Yin, F. Zhao, J. Lin, P. Huang, In vivo three-dimensional multispectral photoacoustic imaging of dual enzyme-driven cyclic cascade reaction for tumor catalytic therapy. *Nat. Commun.* **13**, 1298 (2022).

63. A. Yuan, X. Qiu, X. Tang, W. Liu, J. Wu, Y. Hu, Self-assembled PEG-IR-780-C13 micelle as a targeting, safe and highly-effective photothermal agent for in vivo imaging and cancer therapy. *Biomaterials* **51**, 184–193 (2015).

64. Y. Wang, H. Bai, Y. Miao, J. Weng, Z. Huang, J. Fu, Y. Zhang, J. Lin, D. Ye, Tailoring a near-infrared macrocyclization scaffold allows the control of in situ self-assembly for photoacoustic/PET bimodal imaging. *Angew. Chem. Int. Ed. Engl.* **61**, e202200369 (2022).